Research Article

Lianzhi Zhang*[#], Zhangyong Wu*[##], Tingyou Wang and Ziyong Mo

The influence of preparation of nano-ZrO_2/α-Al_2O_3 gradient coating on the corrosion resistance of 316L stainless steel substrate

https://doi.org/10.1515/secm-2022-0185
received October 12, 2022; accepted February 01, 2023

Abstract: Generally, 316L stainless steel instrumentation tubes working in a humid environment with a large amount of Cl^- all the year round have serious corrosion problems, so the stainless steel substrate should be gradiently coated with nano-ZrO_2/α-Al_2O_3 slurry. In this article, the slender 316L stainless steel tube was first ground by magnetorheological fluid and then coated with the slurry, which can not only increase the contact area between the coating and the substrate but also prevent the generation of new substances that have adversely affected the adhesion of the coating. The properties of the samples were characterized and analyzed; the results showed that the substrate ground by magnetorheological fluid is more favorable for bonding with coating under the grinding conditions that the speed of the tube is 210 rpm, magnetic induction intensity is 40.83 mT, and mass ratio of micron and submicron magnetic particles is 2.3. The coating prepared under the above conditions has uniform thickness, flat surface, and can better inhibit the diffusion of Cr of the substrate to its surface. It can be obtained from corrosion resistance analysis that the coating has the highest self-corrosion potential of −0.016 V and the lowest corrosion current density of 0.491 μA/cm^2, which indicate that the coating has the strongest corrosion resistance. According to the composition analysis of the coating, the composition of the corroded coating is similar to that of the coating itself, but accompanied by a small amount of Fe, which indirectly indicates that the coating is relatively compact, the coating is well bonded with the substrate, and the coating can protect the substrate; thus, the service life of 316L stainless steel instrumentation tubes is extended.

Keywords: magnetorheological grinding, nanocoating technology, corrosion resistance, magnetic abrasive particles, nontraditional processing

1 Introduction

Manufacturing is the main body of industry, one of the power sources of modernization, and it undertakes the important manufacturing tasks of transportation, living materials, and defense equipment; it is not only an essential carrier of emerging technologies but also a booster for its development. Therefore, its development level determines the lifeline of the entire national economy. Since the 1950s, due to the development demands of materials science, high technology, cutting-edge defense products, and scientific research, the update on new products has been accelerated, and products with high strength and cost performance are required. Therefore, products have been required to develop in the direction of high speed, high precision, high reliability, corrosion resistance, high temperature, high pressure, and high power [1–5]. However, machining as a part of manufacturing science and technology is very important for modern manufacturing industries [6], so machining faces a series of severe challenges [7,8]. The importance of nuclear power has become increasingly prominent with the decrease of fossil fuel

---

[#] Lianzhi Zhang, researching mainly on nontraditional machining on magnetic composite materials.

[##] Zhangyong Wu, researching mainly on water-based hydraulic transmission technology and electrohydraulic digital control technology.

*** Corresponding author: Lianzhi Zhang,** Faculty of Mechanical and Electrical Engineering, Kunming University of Science and Technology, Kunming, 650500, China,
e-mail: 18213843652@163.com
*** Corresponding author: Zhangyong Wu,** Faculty of Mechanical and Electrical Engineering, Kunming University of Science and Technology, Kunming, 650500, China,
e-mail: z15812169785@163.com
Tingyou Wang, Ziyong Mo: Faculty of Mechanical and Electrical Engineering, Kunming University of Science and Technology, Kunming, 650500, China

reserves such as coal and oil [9,10]. Currently, lots of slender 316L stainless steel tubes are used in nuclear safety instruments, such as the pressure-inducing tubes in the built-in orifice flowmeter assembly used to measure the small flow of air. Stress corrosion cracks of 316L stainless steel instrumentation tubes are prone because the medium is wet and contains a large number of chloride ions [11–14], which seriously threatens the use safety of nuclear-grade instrumentation tubes. Therefore, nuclear-grade instrumentation tubes are required to have strong corrosion resistance, so manufacturing requirements for nuclear-grade instrumentation tubes are pretty strict.

At present, the internal surface of the 316L stainless steel tube is often processed by cold drawing, sandblasting, laser irradiation, etc. A cold-drawn stainless steel tube is formed by the plastic deformation of the pre-treated hot-rolled stainless steel tube when it goes through a mold having a particular shape and size under the action of drawing force of a hydraulic high-precision cold-drawing machine. Cold drawing is widely used because of its high production efficiency, chipless processing, and high material utilization rate. However, a large amount of plastic deformation is produced during cold drawing, which will cause significant lattice distortion, resulting in the increase of lattice energy, the increase of internal energy of the metal, and generation of residual stresses [15–24], and eventually the increase of hardness while the decrease of toughness. When the residual stresses reach a specific value, the metal will be torn along a specific grain interface, which will result in the cracking of the stainless steel tube. The blasting process enables roughing or smoothing out the inner surface of 316L stainless steel tube according to individual requirements, but the removal of the surface layers and the subsurface work hardening occurs together with changes in mechanical properties and surface activity [25]. In addition, laser beam micromachining (LBM) causes several phenomena that are variations in dislocations and residual stress distributions, formation of different carbide types, and size and shape modification of austenitic grains, and hardening effects [26]. Therefore, it is urgent to explore a suitable and high-quality processing method for the inner surface of the 316L stainless steel tube.

Magnetorheological grinding (MRF) is an emerging surface precision processing technology. Unlike traditional machining methods, the "tool" used in magnetorheological grinding is loose and free-moved magnetic particles, so its grinding has pretty good flexibility [27–32]. In addition, the interaction between magnetic poles and abrasives is noncontact. Therefore, slender tubes can be ground by magnetic abrasives, while that cannot be processed by the conventional method. Furthermore, a mathematical model that can more comprehensively predict the surface roughness value of the inner surface of the tube has not been found in the existing magnetorheological grinding theory, and the grinding is generally carried out with single particle-size magnetic particles. In this article, magnetic abrasives are prepared by high-energy ball milling of micron and submicron ferromagnetic particles and nano-abrasive particles, so magnetic abrasives with a larger shear yield stress, better fluidity, and large hardness can be obtained. Therefore, when constructing a surface roughness prediction model, in addition to considering the influences of the speed of the stainless steel tube and magnetic induction strength on it, the mass ratio of micron and submicron magnetic particles also needs to be taken into account. However, magnetorheological grinding can not change any chemical properties of the tube, so the corrosion resistance of the tube after grinding is poor. If the inner surface of the ground tube is coated with corrosion-resistant nanomaterials, the corrosion resistance of the stainless steel tube can be significantly improved [33–36].

Numerous techniques [37] have been applied to enhance the corrosion resistance of stainless steel. Coating is one of the most efficient surface treatment and modification techniques among them. Alumina is a cost-effective, heat resistant, and chemically durable material and has broad applications as protective coatings for stainless steel in the marine environment [38], but limitation for this ceramic coating results from the inevitable porous structure of alumina allowing oxygen or aqueous medium permeability. Betts [39] attempted to blow cladding Al_2O_3 powder in a 316 stainless steel substrate but received bad results. Tao et al. [40] conducted a continuous immersion test in 3.5 wt% NaCl solution on Al coatings on AZ91D magnesium alloy; the results measured by EIS revealed that the corrosion resistance decreased and the Warburg diffusive impedance increased sharply due to the pitting corrosion at the active sites which were later filled with solution and corrosion products. However, the Al/Al_2O_3 multilayers prepared by evaporation with ion beam-assisted deposition (IBAD) have been successfully applied on CK45 steel by Xue et al. [41], and good corrosion protection has been obtained. Yi's study has shown that Al/Al_2O_3 bilayer coating with a graded interface layer can improve corrosion resistance and surface hardness [42]. However, the most prominent problem in preparing coating on the substrate surface is poor adhesion, which often leads to coating to crack and even spall in application [43–45]. Several techniques have been reported to facilitate the bond strength between resin cement and Y-TZP ceramic [46]. In addition, tribochemical silica coating was suggested as an effective method for bonding [47], but it has been recently criticized for possibility of subcritical crack propagation within zirconia [48]. In the relevant research [49], Al_2O_3 ceramic coating deposited on metallic substrates by plasma spraying has received considerable attention for good corrosion resistance. However, the single Al_2O_3 coating presents porous microstructures and poor bonding. Especially, it often obtained lower bond strength between Al_2O_3 ceramic and the metallic substrate due to their biggest difference in thermal expansion coefficient.

In conclusion, in order to improve the bonding strength between coating and substrate, on the one hand, the substrate needs to be ground in advance, and on the other hand, the coating needs to be gradiently prepared to reduce the stresses in the coating. Therefore, in this article, the slender 316L stainless steel tube was first ground by magnetorheological fluid and then gradiently coated with the prepared nano-ZrO_2/α-Al_2O_3 slurry, which can not only increase the contact area between the coating and the substrate but also prevent the generation of new substances that have adversely affected the adhesion of the coating, eventually improving the bonding strength between the coating and the substrate and achieving the protection of the substrate. In addition, for the parts working in nuclear power plants, the selection of coating materials in terms of good corrosion resistance, and good high-temperature stability, α-Al_2O_3 is the preferred coating material because α-Al_2O_3 has not only good corrosion resistance, good thermal stability, high thermal conductivity, and low thermal expansion coefficient but also is cheap and rich in raw materials. Thermal expansion coefficient of ZrO_2 is between that of 316L stainless steel and that of α-Al_2O_3. Moreover, ZrO_2 has excellent corrosion resistance. Therefore, ZrO_2 is used as transition layer material, which can relieve the generation of stresses during the preparation of coating, so the bonding strength between the coating and the substrate is increased, and eventually, corrosion resistance of the coated sample is improved.

Therefore, in this article, the slender 316L stainless steel tube was first ground by magnetorheological fluid and then gradiently coated with nano-ZrO_2/α-Al_2O_3 slurry; finally, its corrosion resistance is significantly improved.

2 Establishment of surface roughness prediction model by multiple linear regression

The proper magnetic induction intensity is crucial for obtaining a high-precision and high-quality processing surface in magnetorheological grinding. Considering the actual situation of shearing and grinding of the magnetorheological fluid, magnetic particles should include both micron and submicron sizes, so mass ratio ε of micron and submicron magnetic particles has an important influence on the inner surface quality of the tube. In addition, it is also necessary to consider the influence of the speed of the slender tube on the surface quality. Therefore, a surface roughness prediction model can be constructed as shown in equation (1).

$$Sq = Kn^{\beta_1}\overline{B}^{\beta_2}\varepsilon^{\beta_3}, \tag{1}$$

where Sq is the evaluation value of three-dimensional surface roughness of the inner surface of the slender tube; K is the scale coefficient of the model; n is the speed of the slender tube; B is the magnetic induction intensity value; ε is the mass ratio of micron and submicron magnetic particles. The surface roughness values of inner surfaces of slender tubes (substrates) after magnetic grinding are shown in Table 1.

Formula (1) is a nonlinear function. A linear function model of Formula (2) can be obtained by linearizing Formula (1).

$$\lg Sq = \lg K + \beta_1 \lg n + \beta_2 \lg \overline{B} + \beta_3 \lg \varepsilon. \tag{2}$$

Let $y = \lg Sq$, $\beta_0 = \lg K$, $x_1 = \lg n$, $x_2 = \lg \overline{B}$, and $x_3 = \lg \varepsilon$. The simplified linear regression model is shown in equation (3).

Table 1: Surface roughness values of substrates after magnetic grinding

Substrate	**Speed of tube** n/(rpm)	**magnetic induction intensity** B/(mT)	**Mass ratio** ε	**Surface roughness value** Sq/μm
1#	105	96.07	1.5	5.385
2#	210	96.07	9.0	5.813
3#	132	96.07	2.3	5.897
4#	170	96.07	4.0	5.032
5#	210	59.12	4.0	6.799
6#	170	59.12	9.0	5.955
7#	132	59.12	1.5	5.195
8#	105	59.12	2.3	4.634
9#	210	40.83	2.3	6.778
10#	170	40.83	1.5	6.821
11#	132	40.83	9.0	6.510
12#	105	40.83	4.0	6.214
13#	210	29.06	1.5	7.526
14#	170	29.06	2.3	6.874
15#	132	29.06	4.0	6.914
16#	105	29.06	9.0	6.437

$$y = \beta_0 + \beta_1 x_1 + \beta_2 x_2 + \beta_3 x_3. \tag{3}$$

Multiple linear regression equations are constructed as follows:

$$\begin{cases} y_1 = \beta_0 + \beta_1 x_{11} + \beta_2 x_{12} + \beta_3 x_{13} + \delta_1 \\ y_2 = \beta_0 + \beta_1 x_{21} + \beta_2 x_{22} + \beta_3 x_{23} + \delta_2 \\ \vdots \\ y_{16} = \beta_0 + \beta_1 x_{161} + \beta_2 x_{162} + \beta_3 x_{163} + \delta_{16} \end{cases}, \tag{4}$$

where δ_i is the random experimental error. Let

$$Y = \begin{bmatrix} y_1 \\ y_2 \\ \vdots \\ y_{16} \end{bmatrix} X = \begin{matrix} 1 & x_{11} & x_{12} & x_{13} \\ 1 & x_{21} & x_{22} & x_{23} \\ \vdots & \vdots & \vdots & \vdots \\ 1 & x_{161} & x_{162} & x_{163} \end{matrix} \beta = \begin{bmatrix} \beta_0 \\ \beta_1 \\ \beta_2 \\ \beta_3 \end{bmatrix}, \text{ and } \delta = \begin{bmatrix} \delta_1 \\ \delta_2 \\ \vdots \\ \delta_{16} \end{bmatrix}$$

The regression model is

$$Y = X\beta + \delta, \tag{5}$$

where Y is the matrix composed of values obtained after logarithmic transformation for each group of surface roughness values; X is the matrix composed of values obtained after logarithmic transformation for each process parameter; β is the matrix composed of the regression coefficients in the linear regression model; δ is the matrix composed of the random errors.

It is known from the principles of the method of least squares that the least-squares estimation vector $\hat{B}$ can be solved when the residual sum of squares in the linear regression model takes a minimal value.

$$Q = \sum_{i=1}^{n} \delta_i{}^2 = \delta'\delta = (Y - X\beta)'(Y - X\beta). \tag{6}$$

Therefore, the partial derivative of the residual sum of squares with respect to the parameter β to be estimated is zero. That is

$$\frac{\partial Q}{\partial \beta} = -2X'Y + 2X'X\hat{\beta} = 0. \tag{7}$$

Assuming that the matrix $X'X$ exists, the formula (8) can be obtained from formula (7), as follows:

$$\hat{\beta} = (X'X)^{-1}X'Y. \tag{8}$$

Substituting the data in Table 1 into equation (8), the regression coefficients can be obtained as shown in equation (9).

$$\hat{\beta} = \begin{bmatrix} \hat{\beta}_0 \\ \hat{\beta}_1 \\ \hat{\beta}_2 \\ \hat{\beta}_3 \end{bmatrix} = \begin{bmatrix} 0.622 \\ 0.219 \\ -\ 0.198 \\ 0.008 \end{bmatrix}. \tag{9}$$

The regression equation can be determined by equation (9):

$$y = 0.622 + 0.219x_1 - 0.198x_2 + 0.008x_3. \tag{10}$$

Then, the prediction model of surface roughness is:

$$Sq = 10^{0.622} n^{0.219} \overline{B}^{-0.198} \varepsilon^{0.008}. \tag{11}$$

From the index of each process parameter of the prediction model of surface roughness, it can be seen that the importance order of process parameters that affect the microscopic morphology of the inner surface of stainless steel tube is respectively speed of slender tube, magnetic induction intensity, and mass ratio of micron and submicron magnetic particles. The comparison results between the measured and predicted values of the inner surface roughness of the slender tube are shown in Table 2.

It can be seen from Table 2 that the maximum absolute value of the absolute error of the prediction model is 0.922 µm, and the average value of absolute error is −0.34 µm; the maximum absolute value of relative error is 15.6%, and its average value is −4.96%, which indicate that prediction accuracy of the prediction model is good. The model can better reflect the influences of the various process parameters on the micromorphology of the inner surface of the slender tube after magnetic grinding and guide the selection of magnetic abrasive grinding process parameters.

Table 2: Comparison results between the measured and predicted values of inner surface roughness of the slender tube

Substrate	Measured value *Sq*/µm	Predicted value *Sq*/µm	Absolute error	Relative error (%)
1#	5.385	4.700	−0.685	−12.7
2#	5.813	5.569	−0.244	−4.2
3#	5.897	4.975	−0.922	−15.6
4#	5.032	5.280	0.248	4.9
5#	6.799	6.089	−0.710	−10.4
6#	5.955	5.853	−0.102	−1.71
7#	5.195	5.440	0.245	4.7
8#	4.634	5.211	0.577	12.5
9#	6.778	6.526	−0.252	−3.7
10#	6.821	6.187	−0.634	−9.3
11#	6.510	5.959	−0.551	−8.5
12#	6.214	5.629	−0.585	−9.4
13#	7.526	6.931	−0.595	−7.9
14#	6.874	6.664	−0.210	−3.1
15#	6.914	6.330	−0.584	−8.4
16#	6.437	6.063	−0.374	−5.8

3 Materials and method

The monoclinic ZrO_2 (20 nm), α-Al_2O_3 (30 nm), Fe_3O_4 (80 mesh), Fe_3O_4 (800 mesh), cetyltrimethylammonium bromide (CTAB), sodium carboxymethyl cellulose (CMC) and other reagents used in the experiments are all analytically pure and were purchased from high-quality zirconium nanomaterials Co.,Ltd. in Suzhou.

3.1 Magnetorheological grinding of a slender 316L stainless steel tube

Fe_3O_4/ZrO_2 magnetorheological fluid was prepared by a double planetary ball mill. The magnetic block supported by a self-made frame was fixed on the skateboard of the CY6140 ordinary lathe by the magnetic base. One end of the slender tube was sealed with a cap, and then, the magnetorheological fluid was injected into the slender tube with a syringe, and the other was sealed and clamped on the machine tool spindle. The tube was cut into half from the middle part with a wire electric discharge machine after magnetorheological grinding. Half of it was used to measure the surface roughness value of the sample. The other half was used for slurry coating experiments. The behavior of magnetic abrasive particles in a magnetic field is shown in Figure 1(a). The grinding schematic diagram of magnetic abrasive particles is shown in Figure 1(b).

3.2 Preparation of nano-ZrO_2/α-Al_2O_3 gradient coating

The ground substrate was first pretreated before the slurry was coated. The dust on the substrate surface was first removed with diluted alcohol, and the rust on the substrate surface was removed with diluted oxalic acid. After cleaning and drying the substrate, the coating of the slurry can be carried out. The CMC, ZrO_2, and α-Al_2O_3 were mixed well using an electric stirrer. The slurry could be prepared after the mixed mixture of CMC, ZrO_2, and α-Al_2O_3 was milled by a double planetary ball mill for some time. The slurry was gradiently coated on the substrate surface by the wetting method; a schematic diagram of gradient coating is shown in Figure 2. The slurry was further dried in a constant-temperature drying oven at 60°C for 30 min after being naturally dried and then held in a chamber resistance furnace at 310°C for 1 h, so nano-ZrO_2/α-Al_2O_3 gradient coating could be prepared.

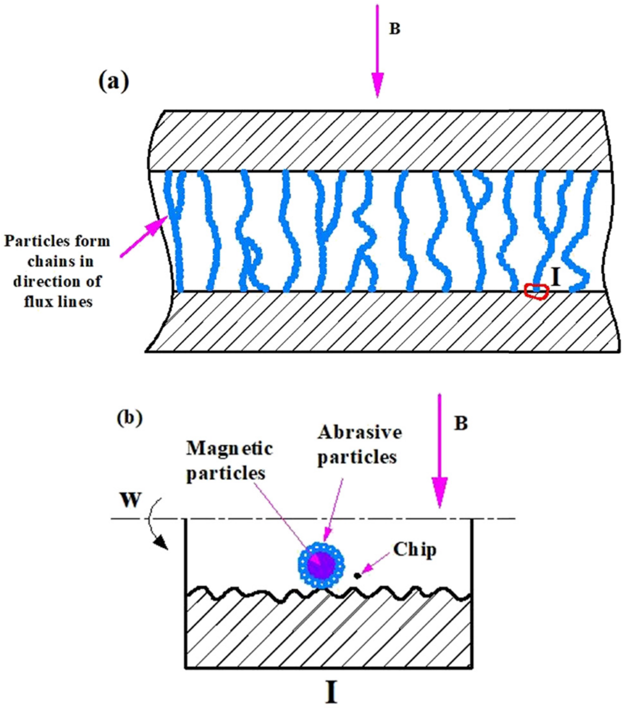

Figure 1: Grinding mechanism of magnetic abrasive particles: (a) behavior of magnetic abrasive particles in magnetic field, (b) grinding schematic diagram of magnetic abrasive particles.

The coated samples were cut into 10 mm in length with a wire electric discharge machine and used for corrosion test analysis in a CHI760e electrochemical workstation. The photo of the electrochemical workstation is shown in Figure 3. The green collet is connected to the working electrode, the red collet is connected to the platinum sheet counter electrode, and the white collet is connected to the silver/silver chloride reference electrode. Finally, the surface and cross-sectional morphologies of samples were observed using a high-resolution field emission scanning electron microscope (FESEM).

4 Results and discussions

4.1 Surface roughness analysis

The microscopic morphologies of substrates after magnetic grinding are shown in Figure 4. It can be seen that the surface roughness value of substrate 8# (Figure 4(h)) is 4.634 µm, which is the minimum value. The surface roughness value of substrate 13# (Figure 4(m)) is 7.526 µm, which is the maximum value. From the perspective of the fluctuation range of the surface roughness value, the

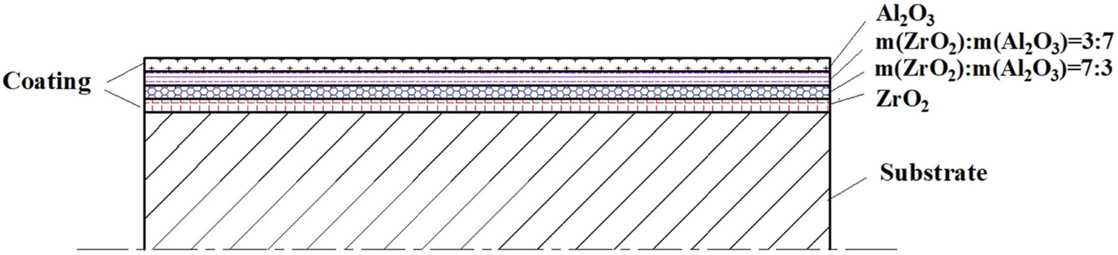

Figure 2: Schematic diagram of ZrO_2/α-Al_2O_3 gradient coating.

fluctuation range of the surface roughness value of substrate 8# is the smallest in the range of −20.069 to 8.235 µm; in contrast, the fluctuation range of the surface roughness value of substrate 6# is the largest in the range of −61.793 to 7.625 µm; it can also be seen that substrates with smaller surface roughness values are 1#, 4#, 7#, 8#, and the fluctuation range of their surface roughness values is small, all fluctuating around −25 to 18 µm. Substrates with larger surface roughness values are 5#, 10#, 13#, 14#, 15#, and their fluctuation range is more extensive, fluctuating around −34–38 µm. Surface roughness values of substrate 2#, substrate 3#, substrate 6#, substrate 9#, substrate 11#, substrate 12#, and substrate 16# are neither too large nor too small; the fluctuation range is quite different. The surface quality of ground substrate 8# is the best, and its fluctuation range is the smallest under the grinding conditions that the speed of tube is 105 rpm, magnetic induction intensity is 59.12 mT, and mass ratio of micron and submicron magnetic particles is 2.3.

The surface roughness effect curve is used to intuitively express the influence of key parameters on the ground surface roughness, as shown in Figure 5. It can be seen from Figure 5 that the surface roughness of the tube wall increases with the increase in speed of the tube because the grinding pressure of magnetic abrasives on the tube wall increases with the increase of speed of the tube, and finally, the scraping effect of magnetic abrasives is enhanced, the rougher cutting lines are left on the substrate surface while removing the convex and concave layers, so the surface roughness of the tube wall increases accordingly; the surface roughness is the minimum at 105 rpm. It can also be seen that the surface roughness of the tube wall decreases with the increase of magnetic induction intensity because the grinding pressure of magnetic abrasives increases with the increase of magnetic induction intensity, and finally grinding ability of magnetic abrasives is enhanced. However, an increase of low magnetic induction intensity will not produce excessive grinding pressure which will cause serious scratches on the tube wall, so the surface roughness of the tube wall decreases with the increase of magnetic induction intensity; the surface roughness is the minimum at 96.07 mT. In addition, it can also be seen that the surface roughness of the tube wall decreases first and then increases with the increase of the mass ratio of micron and submicron magnetic particles; the reason is that the increase of the mass ratio is equivalent to the increase of the number of larger-size magnetic particles, so grinding pressure of magnetic abrasives on tube wall increases under the effect of the magnetic field, and finally grinding ability of magnetic particles is enhanced, so the surface roughness shows a downward trend, but the scraping effect of magnetic abrasives on tube wall is too strong with the further increase of mass ratio, which will cause surface roughness of tube

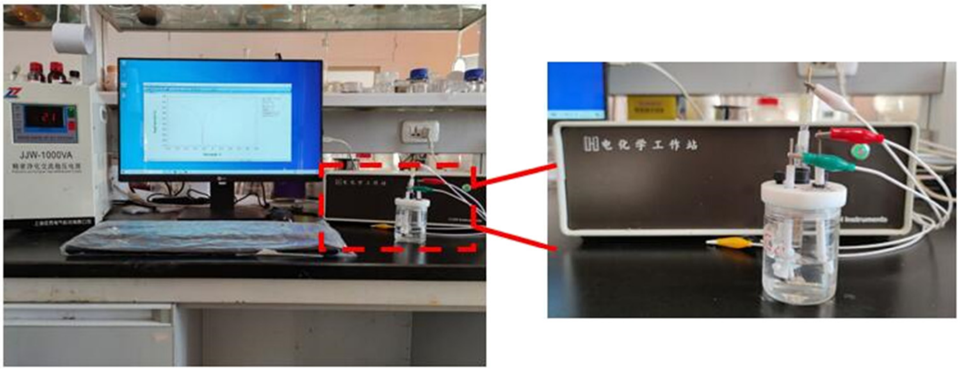

Figure 3: Photo of CHI760e electrochemical workstation.

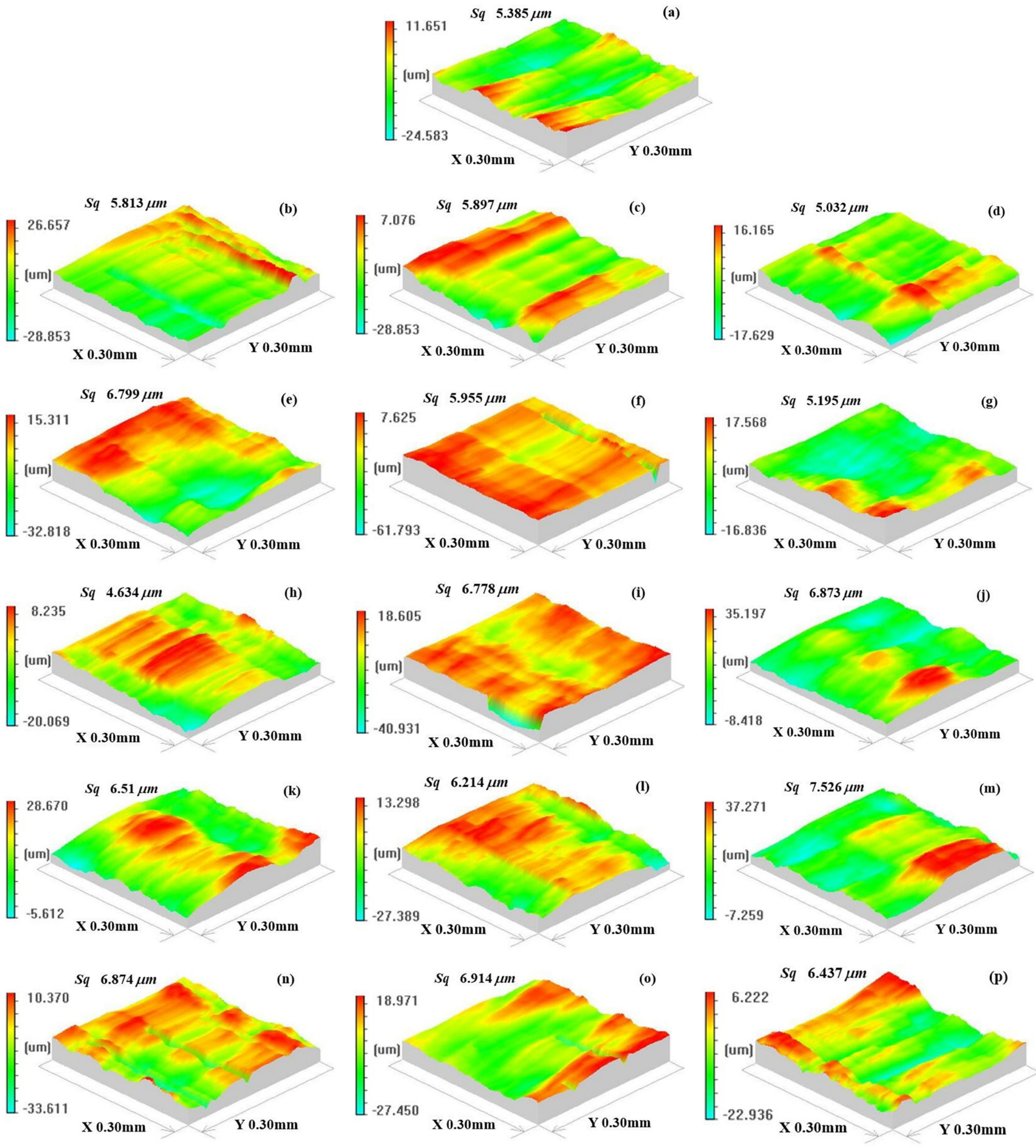

Figure 4: Microscopic morphologies of substrates after magnetic grinding: (a) substrate 1#; (b) substrate 2#; (c) substrate 3#; (d) substrate 4#; (e) substrate 5#; (f) substrate 6#; (g) substrate 7#; (h) substrate 8#; (i) substrate 9#; (j) substrate 10#; (k) substrate 11#; (l) substrate 12#; (m) substrate 13#; (n) substrate 14#; (o) substrate 15#; (p) substrate 16#.

wall to increase. It can be seen that the surface roughness of the tube wall is minimum when the mass ratio of micron and submicron magnetic particles is 2.3.

The surface morphologies of coated sample 2#, coated sample 8#, coated sample 9#, and coated sample 13# are shown in Figure 6. The surface roughness values of the coated samples were compared with that of substrates, respectively; the comparison results are shown in Table 3. The smaller the surface roughness value of the substrate, the smaller the surface roughness value of the corresponding

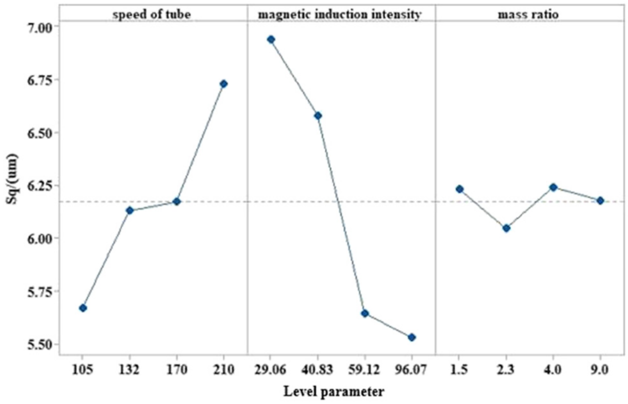

Figure 5: The surface roughness effect curve.

Table 3: Comparison of surface roughness values of inner walls of slender 316L stainless steel tubes before and after coating

Sample	Substrate Sq/μm	The coated sample Sq/μm	Sample	Substrate Sq/μm	The coated sample Sq/μm
2#	5.813	4.381	9#	6.778	4.051
8#	4.634	3.758	13#	7.526	6.194

coated sample. It can also be seen that the greater the surface roughness value of the substrate, the more significant the decrease of the surface roughness value of the corresponding coated sample, and the coating effect is better.

4.2 Morphological analyses in field emission scanning electron microscope

Surface morphologies of substrates obtained under different magnetic grinding conditions are shown in Figure 7. It can be seen from Figure 7 that the surface morphology of substrate 8# (Figure 7(b)) is the flattest compared with other substrates, which means magnetic abrasives have the best grinding effect on substrate 8#; that is, its surface quality is the best under the grinding conditions that speed of tube is 105 rpm, magnetic induction intensity is 59.12 mT, and mass ratio of micron and submicron magnetic particles is 2.3. It can also be seen from Figure 7 that the surface morphology of substrate 13# (Figure 7(d)) is the roughest compared with other substrates, which means magnetic abrasives have the worst grinding effect on substrate 13#; that is, its surface quality is the worst under the grinding conditions that speed of tube is 210 rpm, magnetic induction intensity is 29.06 mT, and mass ratio of micron and submicron magnetic particles is 1.5. The surface quality of substrate 8# is superior to that of substrate 2#, that of substrate 2# is superior to that of substrate 9#, and that of substrate 9# is superior to that of substrate 13# among the four substrates shown in Figure 7.

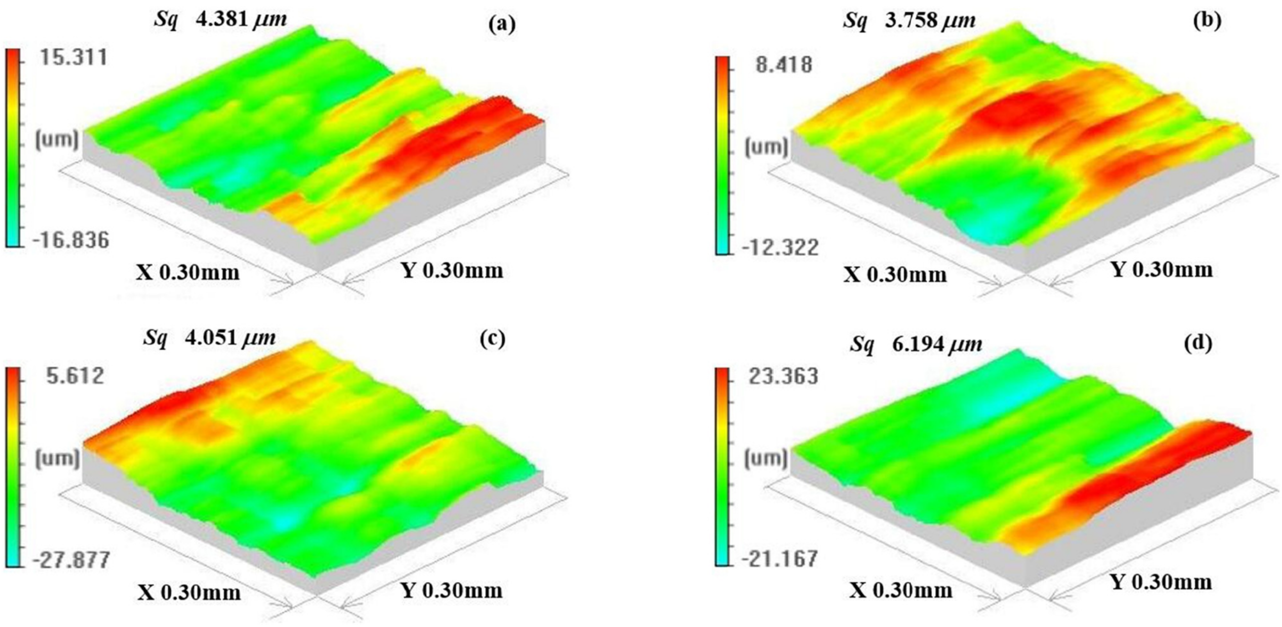

Figure 6: Microscopic morphologies of the coated samples: (a) the coated sample 2#; (b) the coated sample 8#; (c) the coated sample 9#; (d) the coated sample 13#.

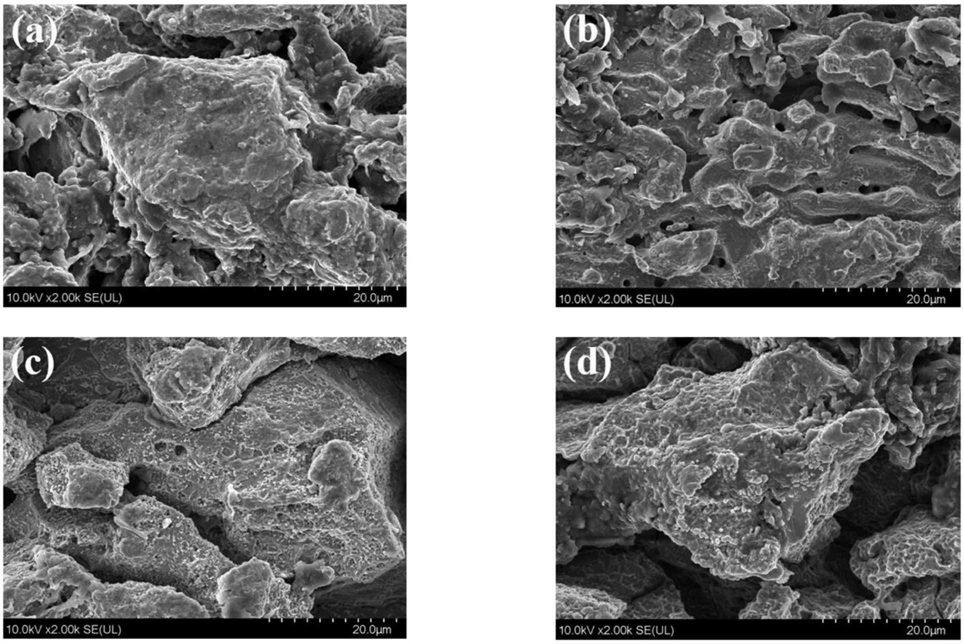

Figure 7: FESEM photos of surface morphologies of substrates: (a) substrate 2#, (b) substrate 8#, (c) substrate 9#, (d) substrate 13#.

The surface morphologies of the coated samples are shown in Figure 8. It can be seen that the coated sample 8# (Figure 8(b)) has the most severe cracks, while the coated sample 2# (Figure 8(a)) and the coated sample 9# (Figure 8(c)) have fewer cracks. The coated sample 13# (Figure 8(d)) has almost no cracks but a large number of holes. The reason is that the surface roughness value of substrate 8# is the smallest, that is 4.634 μm, so the contact area between the coating and substrate 8# is small, which will result in low bonding strength between the coating and the substrate. Therefore, coated sample 8# is prone to cracking during sintering. Surface roughness value of substrate 9# is more considerable, that is 6.778 μm, and the contact area between the coating and substrate 9# is larger, which makes the bond strength between the coating and the substrate significantly stronger; therefore, coated sample 9# rarely cracked after sintering. It can be seen from Table 3 that the surface roughness value of substrate13# is the largest, that is 7.526 μm, and the substrate surface is highly uneven; therefore, dirt and air bubbles can easily remain in concave areas, which will result in incomplete penetration of the slurry into the concave areas, so many holes exist.

The cross-sectional morphologies of the coated samples are shown in Figure 9. It can be seen from Figure 9 that the bottom part of the coated sample 2# (Figure 9(a)) is a porous layer and the top part is a loose layer; the bonding between coating and substrate 2# is poor. Taking point A on the coating surface for spectrogram analysis, it can be seen that the atomic fractions of Zr and Al on the coating surface are low. The structure of coated sample 8# (Figure 9(c)) is loose and accompanied by spalling of the coating; its cross-sectional line scan EDS analysis is shown in Figure 9(d). From Figure 9(e), it can be seen that structure of the coated sample 9# is continuous and compact without defects such as holes, the coating thickness is uniform, the coating surface is flat, and the coating is well bonded with substrate 9#; its cross-sectional line scan EDS analysis is shown in Figure 9(f). It is shown in Figure 9(i) that the content of Cr on the surface of coated sample 9# is lower than that of coated sample 8#, which indirectly indicates that coated sample 9# is compacter, so coated sample 9# can better inhibit diffusion of Cr of the substrate to the coating surface. It can be seen from Figure 9(g) that the structure of coated sample 13# is not only rough and loose but also has a large number of holes, which are caused by the considerable surface roughness value of substrate13#. The spectral analysis of the G point on the surface of coated sample 13# is shown in Figure 9(h), which shows that atomic fractions of Zr and Al on the coating surface are high.

4.3 The corrosion resistance analyses

The polarization curves of the substrates and the coated samples in 3.5% NaCl solution are shown in Figure 10. According to the curves shown in Figure 10, self-corrosion potential and corrosion current density of each

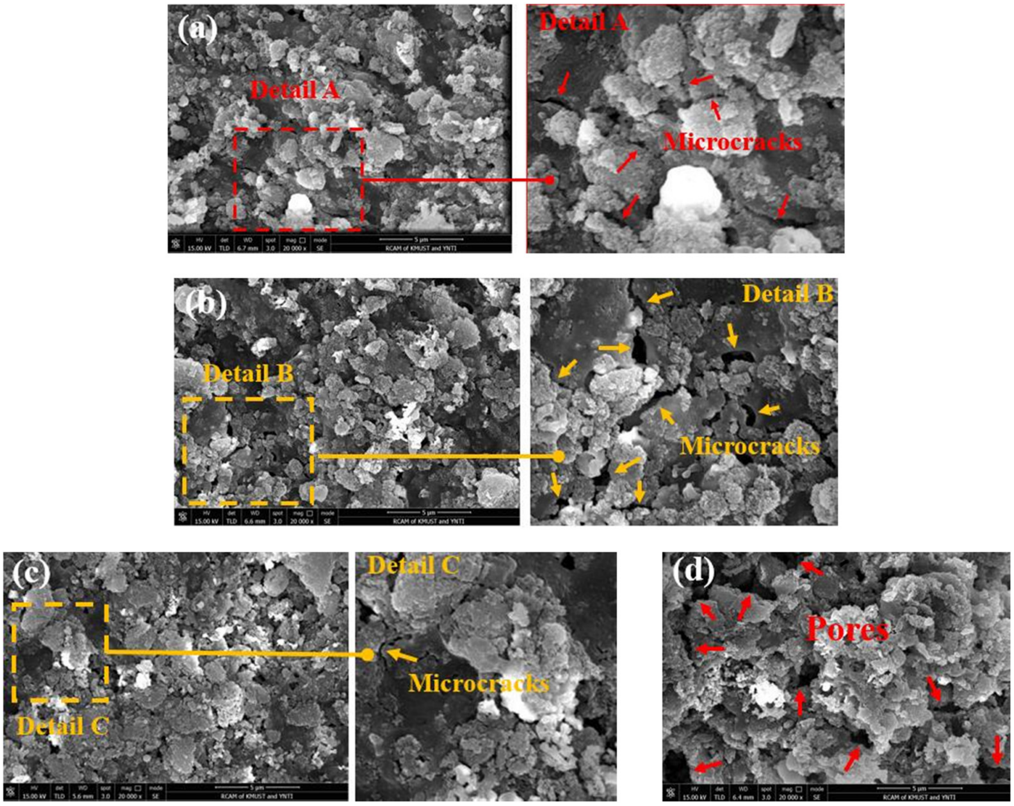

Figure 8: FESEM photos of surface morphologies of the coated samples: (a) coated sample 2#, (b) coated sample 8#, (c) coated sample 9#, and (d) coated sample 13#.

sample can be calculated as shown in Table 4. It can be seen from Table 4 that the self-corrosion potential of the coated samples is significantly increased compared with the substrate, which indicates that the corrosion resistance of the sample can be greatly improved by coating gradiently with the prepared nano-$ZrO_2/\alpha\text{-}Al_2O_3$ slurry after magnetic grinding. Phosphating the surface of the substrate though resulted in crack-free sol–gel coatings, anodic polarization in NaCl solution revealed that current increases with the increase of potential [50,51]; generally speaking, larger corrosion current density usually means higher corrosion rate and worse corrosion resistance [52], so phosphating only offers limited protection for substrate. In addition, phosphating has serious environmental problems because of containing a large number of heavy metal ions such as phosphorus, zinc, manganese, and nickel that cannot be biodegradable, and its energy consumption is large and use cost is high. Therefore, there are many deficiencies in phosphating to improve the corrosion resistance of the substrate. In literature[53], the generation of iron oxides ($Fe_2O_3/Fe_3O_4/FeO$) on steel surfaces had adversely affected the adhesion of the coating during thermal and plasma sprayed coatings; in addition, thermal spraying will not only cause thermal deformation of the workpiece but also produce many harmful substances. However, in this article, the composition of the substrate will not be changed after magnetic grinding; therefore, the generation of new substances that have adversely affected the adhesion of the coating can be prevented. It can be seen from Table 4 that the self-corrosion potential of the coated sample 9# is the highest, that is −0.016 V. In the relevant research [54], the E_{corr} value of Al_2O_3 coated stainless steel was −0.06 V, and its I_{corr} value was 45.5 $\mu A/cm^2$; it can be seen that the I_{corr} value is too large, and obviously, the I_{corr} of the single Al_2O_3 coating increased by 2 orders of magnitude higher than that of $ZrO_2/\alpha\text{-}Al_2O_3$ gradient coating in this article. In addition, in literature [55], sol–gel Al_2O_3 coatings on mild steel/plain carbon steel exhibited limited protection to the substrate. The above conclusions indicate that the corrosion resistance of single Al_2O_3 coating is poor because of a large number of loose structures such as pores caused by its low inherent compactness. The composition of $ZrO_2/\alpha\text{-}Al_2O_3$ gradient coating in this article changes gradiently from inside to outside; that is, the Al_2O_3 content increases gradually from inside to outside, and the thermal expansion coefficient of the coating is

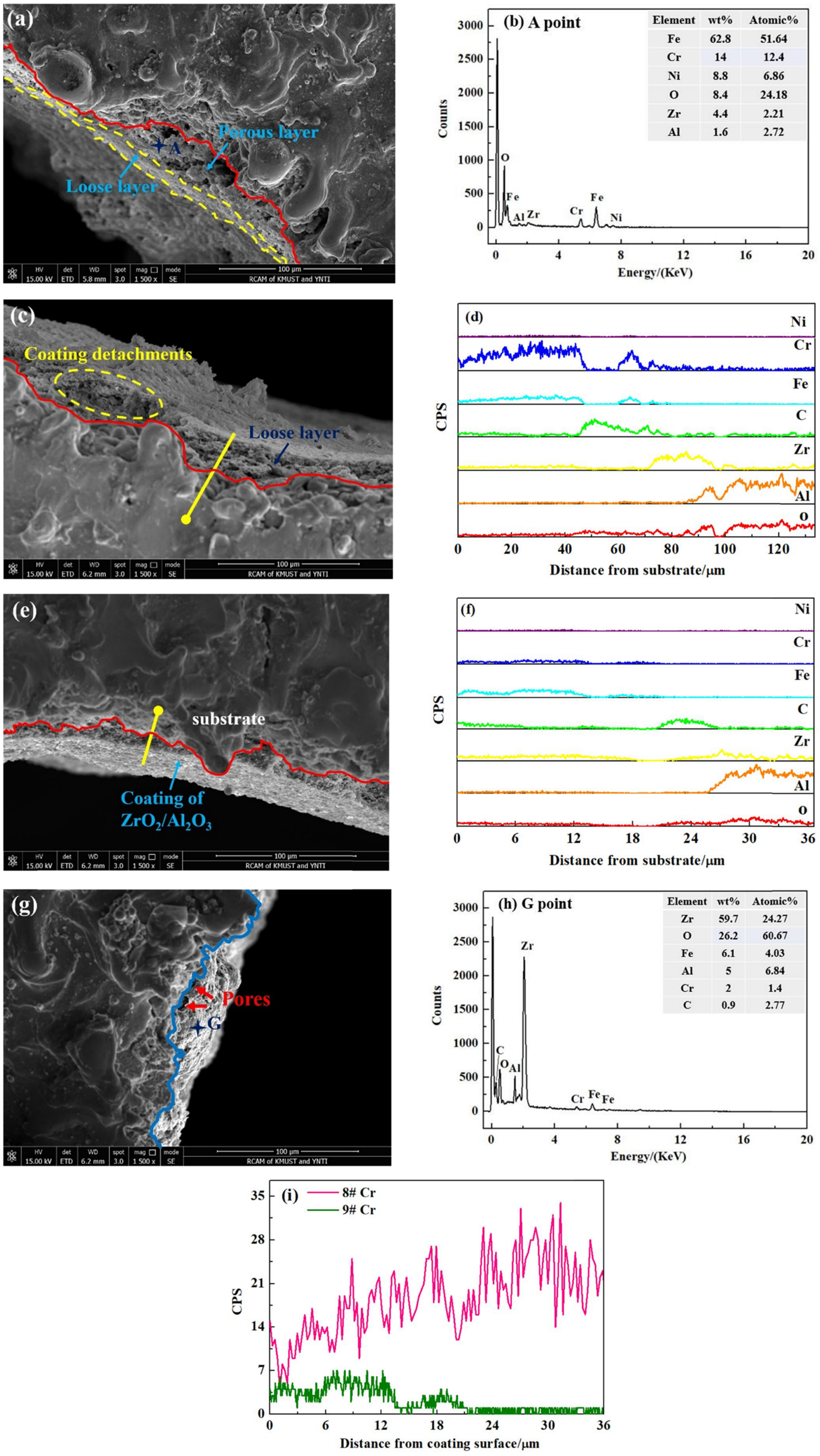

Figure 9: FESEM photos of cross-sectional morphologies and EDS spectra of the coated samples: (a) FESEM photo of coated sample 2#, (b) EDS spectrogram of point A on the surface of coated sample 2#, (c) FESEM photo of coated sample 8#, (d) line scan graph of coated sample 8#, (e) FESEM photo of coated sample 9#, (f) line scan graph of coated sample 9#, (g) FESEM photo of coated sample 13#, (h) EDS spectrogram of point G on the surface of coated sample 13#, and (i) comparative analysis of line scan between coated sample 8# and coated sample 9#.

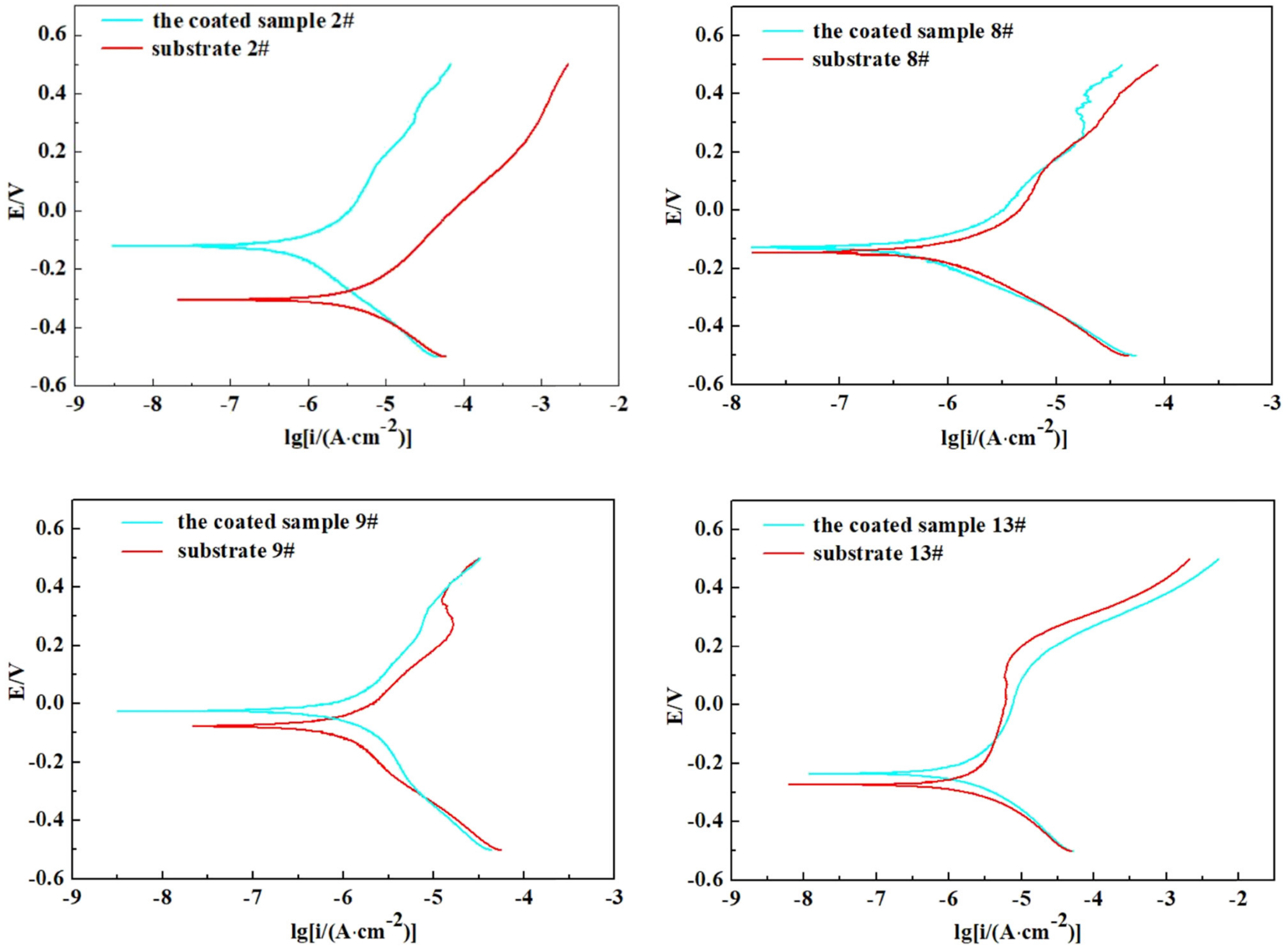

Figure 10: Polarization curves of the substrates and the coated samples in 3.5% NaCl solution.

reduced gradually from inside to the outside, thus reducing thermal stress in the coating, making bonding strength stronger between the coating and the substrate, and making the coating has stronger corrosion resistance. Corrosion current density of the coated samples is generally smaller than that of the substrates according to corrosion current density calculation results. The corrosion current density of coated sample 9# is the smallest, that is 0.491 μA/cm^2, which shows the lowest corrosion rate and indicates that the corrosion resistance of coated sample 9# is the best. However, the corrosion current density of the coated sample 13# is the highest, that is 1.4 μA/cm^2, which indicates that the corrosion rate is the fastest and the corrosion resistance is the worst.

The cross-sectional morphologies of the substrates and the coated samples after corroding in 3.5% NaCl solution are shown in Figure 11. It can be seen that the substrates are prone to cracks (Figure 11(a)) and holes (Figure 11(e)) after corroding; the corroded surface is rough (Figure 11(h)), and the corrosion is more severe. In comparison, the coated

Table 4: Electrochemical parameters of the substrates and the coated samples in 3.5% NaCl solution

Sample	Self-corrosion Potential/V	Corrosion current density /(μA/cm^2)	Sample	Self-corrosion Potential/V	Corrosion current density/(μA/cm^2)
substrate 2#	−0.300	3.380	the coated sample 2#	−0.106	0.881
substrate 8#	−0.146	0.817	the coated sample 8#	−0.126	0.526
substrate 9#	−0.082	0.925	the coated sample 9#	−0.016	0.491
substrate 13#	−0.272	1.870	the coated sample 13#	−0.231	1.400

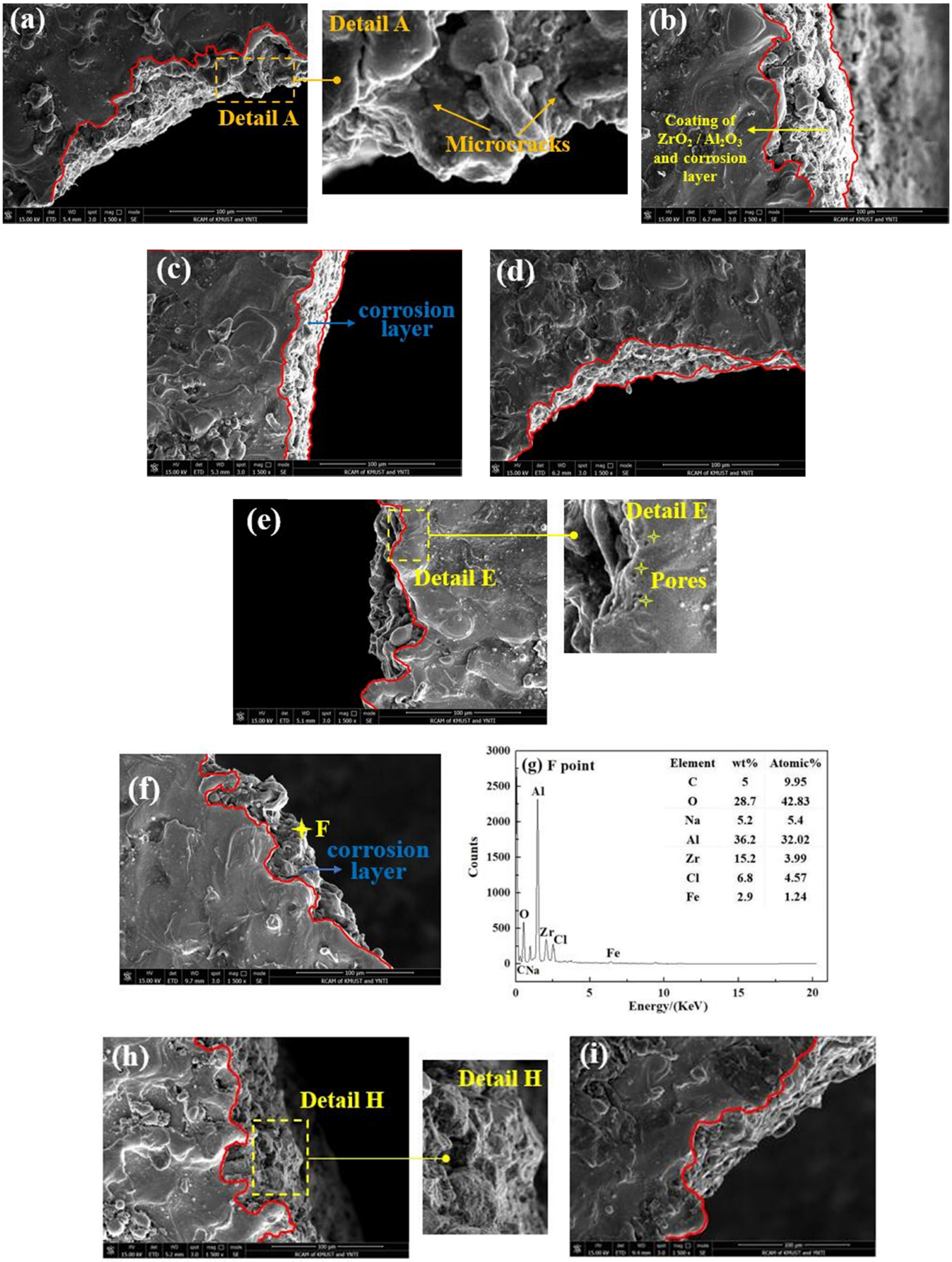

Element	wt%	Atomic%
C	5	9.95
O	28.7	42.83
Na	5.2	5.4
Al	36.2	32.02
Zr	15.2	3.99
Cl	6.8	4.57
Fe	2.9	1.24

Figure 11: FESEM photos of the cross-sectional morphologies of the substrates and the coated samples after corroding: (a) substrate 2#, (b) the coated sample 2#, (c) substrate 8#, (d) the coated sample 8#, (e) substrate 9#, (f) the coated sample 9#, (g) EDS spectrogram of point F on the corroded surface of the coated sample 9#, (h) substrate 13#, and (i) the coated sample 13#.

samples after corroding have fewer corrosion defects because of the substrates coated with more corrosion-resistant $ZrO_2/\alpha\text{-}Al_2O_3$ gradient coating. It can also be seen that coated sample 2# (Figure 11(b)), coated sample 8# (Figure 11(d)), and coated sample 13# (Figure 11(i)) after corroding have many dense microholes compared with coated sample 9# (Figure 11(f)), while the coated sample 9# after corroding has few defects. In addition, taking point F on the corroded surface of the coated sample 9# for spectrogram analysis (Figure 11(g)), the result showed that the composition of the corroded coating is similar to that of the coating itself, but accompanied by a small amount of Fe, which indirectly indicates that the coating is relatively compact, the coating is well bonded with substrate 9#, and the coating can protect the substrate.

5 Conclusion

In this article, the inner wall of a slender 316L stainless steel tube was ground by magnetorheological fluid, and corrosion resistance of substrates and the coated samples in a salt environment was deeply studied. The research results are as follows:

(1) A surface roughness prediction model was constructed by multiple linear regression, and the maximum relative error between the predicted values of the prediction model and the experimental values is 15.6%, which indicates that the prediction accuracy of the prediction model is good and the prediction model can guide the selection of magnetic abrasive grinding process parameters.
(2) According to the surface roughness values of samples after magnetic grinding and the FESEM analysis, the surface roughness value of ground substrate 8# is the smallest, that is 4.634 µm; under the grinding conditions that the speed of tube is 105 rpm, magnetic induction intensity is 59.12 mT, and mass ratio of micron and submicron magnetic particles is 2.3.
(3) It can be obtained from the surface roughness effect curve that the surface roughness of the tube wall increases with the increase of speed of the tube, decreases with the increase of magnetic induction intensity, and decreases first and then increases with the increase of the mass ratio of micron and submicron magnetic particles.
(4) It can be seen from the cross-sectional morphologies of the coated samples that the structure of the coated sample 9# is continuous and compact, and the coating thickness is uniform, the coating surface is flat, the coating is well bonded with substrate 9#, which indirectly indicate that the substrate ground by magnetorheological fluid is more favorable for bonding with coating under the grinding conditions that speed of tube is 210 rpm, magnetic induction intensity is 40.83 mT, and mass ratio of micron and submicron magnetic particles is 2.3.
(5) It can be obtained from corrosion resistance analysis that the self-corrosion potentials of the coated samples are both significantly increased, and the corrosion current densities of the coated samples are generally reduced, which indicates that the corrosion resistance of the coated samples has been improved. Therein, the self-corrosion potential of coated sample 9# is the highest, that is −0.016 V, and the corrosion current density of the coated sample 9# is the smallest, which is 0.491 $\mu A/cm^2$, which indicates that the corrosion resistance of the coated sample 9# is the best. The composition of the corroded surface of coated sample 9# is similar to that of the coating itself but accompanied by a small amount of Fe, which indirectly indicates that the coating is relatively compact, the coating is well bonded with substrate 9#, and the coating can protect the substrate.

Acknowledgments: This work was financially supported by the Natural Science Foundation of China (51165012). The Analytical and Testing Centers at Kunming University of Science and Technology is appreciated.

Conflict of interest: The authors declare no conflict of interest.

Data availability statement: All data, models, and code generated or used during the study appear in the published article.

References

[1] Zeng YH, Yang FF, Chen ZN, Guo EY, Gao MQ, Wang XJ, et al. Enhancing mechanical properties and corrosion resistance of nickel-aluminum bronze via hot rolling process. J Mater Sci Technol. 2021;61:186–96.
[2] Xu JZ, Liu MJ, Yang H, Fu TY, Tian JD. The enhancement of filament winding in marine launching rubber gasbag. Sci Eng Compos Mater. 2019;26:540–9.
[3] Mani SP, Agilan P, Kalaiarasan M, Ravichandran K, Meng Y. Effect of multilayer CrN/CrAlN coating on the corrosion and contact resistance behavior of 316L SS bipolar plate for high

temperature proton exchange membrane fuel cell. J Mater Sci Technol. 2022;97:134–46.
[4] Davim JP, editor. Mechanical and industrial engineering. Switzerland: Springer; 2022.
[5] Wang JH, Lyu BH, Jiang L, Shao Q, Deng CB, Zhou YF, et al. Chemistry enhanced shear thickening polishing of Ti–6Al–4V. Precis Eng. 2021;72:59–68.
[6] Davim JP, editor. Machining: Fundamentals and recent advances. London: Springer; 2008.
[7] Coll M, Fontcuberta J, Althammer M, Bibes M, Boschker H, Calleja A, et al. Towards oxide electronics: A roadmap. Appl Surf Sci. 2019;482:1–93.
[8] Wu WL, Huang H, Chen Z. Dough moulding compound reinforced silicone rubber insulating composites using polymerized styrene butadiene rubber as a compatibilizer. Sci Eng Compos Mater. 2019;26:209–14.
[9] Proust E, Williams LG, Ahnert C. The important role of nuclear in a low-carbon world: The view of the European Nuclear Society's High Scientific Council. International Conference on Climate Change and The Role of Nuclear Power; 2019.
[10] Gunduz O, Bilgi E. The potential of nuclear energy in minimizing greenhouse gas emissions: A case study from Turkey. Water Environ Syst. 2018;34:110–8.
[11] Fournier L, Savoie M, Delafosse D. Influence of localized deformation on A 286 austenitic stainless steel stress corrosion cracking in PWR primary water. J Nucl Mater. 2007;366:187–97.
[12] Parande G, Manakari V, Kopparthy SDS, Gupta M. A study on the effect of low-cost eggshell reinforcement on the immersion, damping and mechanical properties of magnesium–zinc alloy. Compos Part B-Eng. 2020;182:107650.
[13] Was GS, Ampornrat P, Gupta G, Teysseyre S, West EA, Allen TR, et al. Corrosion and stress corrosion cracking in supercritical water. J Nucl Mater. 2007;371:176–201.
[14] Li P, Li C, Dong HG, Wu BS, Ma YT, Zou CZ, et al. Vacuum diffusion bonding of TC4 titanium alloy to 316L stainless steel with $AlCoCrCuNi_2$ high-entropy alloy interlayer. J Alloy Compd. 2022;909:164698.
[15] Kapustová M, Sobota R. The research of influence of strain rate in steel tube cold drawing processes using FEM simulation. Mater Sci Forum. 2019;952:235–42.
[16] Parilák U, Burik P, Bella P, Kejzlar P. Texture evolution during cold drawing of steel tube with respect to the stress - Strain state. Defect Diffus Forum. 2020;405:115–20.
[17] Shu G, Jin X, Zhang YQ, Gu YY, Zheng BF, Jiang QL. Experimental and numerical study of cold-drawn duplex stainless steel square tube columns. J Constr Steel Res. 2019;156:155–66.
[18] Dai J, Li W, Chu Z. Microstructure evolution of cold pilgering stainless steel tubes. Adv Mater Sci Eng. 2020;6:1–8.
[19] Huang S, Hu J, Li XY. Influence of deformation degree at cold drawing on structure-properties relationship of a Fe-Ni-Cr superalloy. J Alloy Compd. 2022;930:167407.
[20] Liu HL, Zhang MC, Xu M, Meng Y, Xu GH, Ta N, et al. Microstructure evolution dependence of work-hardening characteristic in cold deformation of a difficult-to-deform nickel-based superalloy. Mat Sci Eng A. 2020;140:280–6.
[21] Liu SC, Gao Y, Lin ZL, Guo SS, Zhang XB, Yin XJ. Microstructure and properties after deformation and aging process of A286 superalloy. Rare Met. 2019;38:864–70.
[22] Ma XG, Chen J, Wang XH, Xu YJ, Xue YJ. Microstructure and mechanical properties of cold drawing CoCrFeMnNi high entropy alloy. J Alloy Compd. 2019;795:45–53.
[23] Jin ZH, Gumbsch P, Albe K, Ma E, Lu K, Gleiter H, et al. Interactions between non-screw lattice dislocations and coherent twin boundarics in face-centered cubic metals. Acta Mater. 2008;56:1126–35.
[24] Gattmah J, Ozturk F, Orhan S. A new development of measurement technique for residual stresses generated by the cold tube drawing process with a fixed mandrel. Int J Adv Manuf Tech. 2020;108:11–2.
[25] Wang FF, Feng LJ, Ma HN, Zhai Z, Liu Z. Influence of nano-SiO_2 on the bonding strength and wear resistance properties of polyurethane coating. Sci Eng Compos Mater. 2019;26:77–83.
[26] Obergfell K, Schulze V, Vöhringer O. Classification of microstructural changes in laser hardened steel surfaces. Mat Sci Eng A. 2003;355:348–56.
[27] Jiang X, Zhang Y, Lu W, Gao S, Liu L, Liu X. Characteristics of shear stress based on magnetorheological fluid flexible fixture during milling of the thin-walled part. Int J Adv Manuf Tech. 2020;108:5–8.
[28] Wang PY, Wang ZJ, Xiang N. Effect of magnetic field on tension–tension side of forming limit diagram in sheet metal forming using a magnetorheological fluid. Int J Adv Manuf Tech. 2021;31:1–15.
[29] Khedkar YM, Bhat S, Adarsha H. A review of magnetorheological fluid damper technology and its applications. Int Rev Mech Eng. 2019;13:256–64.
[30] Jackson MJ, Davim JP, editors. Machining with abrasives. New York: Springer; 2011.
[31] Mangal SK, Kataria M. Characterization of magnetorheological finishing fluid for continuous flow finishing process. J Appl Fluid Mech. 2018;11:1751–63.
[32] Davim JP, editor. Nontraditional machining processes. London: Springer; 2013.
[33] Yin XX, Mu P, Wang QT, Li J. Superhydrophobic ZIF-8-based dual-layer coating for enhanced corrosion protection of Mg alloy. ACS Appl Mater Interfaces. 2020;12:35453–63.
[34] Aamms A, Paf A, Jsb B. Enhancement of corrosion resistance on plasma spray coated mild steel substrate exposed to marine environment. Mater Today. 2019;15:84–9.
[35] Davim JP, Charitidis CA, editors. Nanocomposites. Berlin: Walter de Gruyter; 2013.
[36] Shukla K, Rane R, Alphonsa J, Maity P, Mukherjee S. Structural, mechanical and corrosion resistance properties of Ti/TiN bilayers deposited by magnetron sputtering on AISI 316L. Surf Coat Tech. 2017;324:167–74.
[37] Ansari F, Naderi R, Dehghanian C. Improvement in the corrosion resistance of stainless steel 304L in sodium chloride solution by a nanoclay incorporated silane coating. RSC Adv. 2015;5:706–16.
[38] Chaliampalias D, Vourlias G, Pavlidou E, Stergioudis G, Skolianos S, Chrissafis K. High temperature oxidation and corrosion in marine environments of thermal spray deposited coatings. Appl Surf Sci. 2008;255:3104–11.
[39] Betts JC. The direct laser deposition of AISI316 stainless steel and Cr_3C_2 powder. J Mater Process Tech. 2019;209:5229–38.
[40] Tao YS, Xiong TY, Sun C, Kong LY, Cui XY, Li TF, et al. Microstructure and corrosion performance of a cold sprayed aluminium coating on AZ91D magnesium alloy. Corros Sci. 2020;52:3191–7.

[41] Xue J, Zhao W, Wolf GK. The corrosion properties of Al/Al_2O_3 multilayered coatings on CK45 steel deposited by IBAD. Surf Coat Tech. 2019;187:194–8.

[42] Xu Y, Liang WP, Miao Q, Wang L, Ren BL, Cui SY. Enhanced high temperature corrosion resistance of Al_2O_3/Al composite coating on γ-TiAl alloy. Rare Met Mat Eng. 2018;47:1075–81.

[43] Li X, Weng ZY, Yuan W, Luo XZ, Wong HM, Liu XM. Corrosion resistance of dicalcium phosphate dihydrate/poly(lactic-co-glycolic acid) hybrid coating on AZ31 magnesium alloy. Corros Sci. 2016;102:209–21.

[44] Hoche H, Schmidt J, GroB S, TroBmann T, Berger C. PVD coating and substrate pretreatment concepts for corrosion and wear protection of magnesium alloys. Surf Coat Tech. 2011;205:145–50.

[45] Han B, Gu D, Yang Y, Fang L, Peng GH, Yang CB. Preparation of yttrium-based rare earth conversion coating and its effect on corrosion resistance of AZ91D magnesium alloy. Int J Electrochem Sci. 2017;12:374–85.

[46] Özcan M, Vallittu PK. Effect of surface conditioning methods on the bond strength of luting cement to ceramics. Dent Mater. 2020;19:725–31.

[47] Amaral R, Özcan M, Valandro LF. Microtensile bond strength of a resin cement to glass infiltrated zirconia-reinforced ceramic: the effect of surface conditioning. Dent Mater. 2016;22:283–90.

[48] Zhang Y, Pajares A, Lawn BR. Fatigue and damage tolerance of Y-TZP ceramics in layered biomechanical systems. J Biomed Mater Res B. 2014;71:166–71.

[49] Aghajani H, Valefi Z, Zamani P. Phase composition, microstructure, mechanical properties, and wear performance of nanostructured Al_2O_3 and Al_2O_3-Y_2O_3 coatings deposited by plasma spraying. Appl Surf Sci. 2022;585:1–17.

[50] Giampaolo A, Medina M, Reyes R, Velez M. Zinc phosphate interlayer for sol-gel-derived aluminosilicate coating on AISI1010 carbon steel. Surf Coat Tech. 1997;89:31–7.

[51] Ruhi G, Modi OP, Singh IB. Corrosion behaviour of nano structured sol-gel alumina coated 9Cr-1Mo ferritic steel in chloride bearing environments. Surf Coat Tech. 2009;204:359–65.

[52] Ascencio M, Pekguleryuz M, Omanovic S. Corrosion behaviour of polypyrrole-coated WE43 Mg alloy in a modified simulated body fluid solution. Corros Sci. 2018;133:261–75.

[53] Maitre A, Denoirjean A, Fauchais P, Lefort P. Plasma-jet coating of preoxidized XC38 steel: Influence of the nature of the oxide layer. Phys Chem Chem Phys. 2002;4:3887–93.

[54] Yu JJ, Liu SY, Li F, Wang TH. Na_2SiO_3/Al_2O_3 composite coatings on 304 stainless steels for enhanced high temperature oxidation inhibition and chloride-induced corrosion resistance. Surf Coat Tech. 2017;309:1089–98.

[55] Crespo MAD, Murillo AG, Torres-Huerta AM, Yanez-Zamora C, Carrillo-Romo FDJ. Electrochemical behaviour of ceramic yttria stabilized zirconia on carbon steel synthesized via sol-gel process. J Alloy Compd. 2009;483:437–41.